An efficient headland-turning navigation system for a safflower picking robot

Guomin Gao,[1] Hui Guo,[1] Jing Zhang,[1,2] Zhenguo Zhang,[1] Tianlun Wu,[1] Hao Lu,[1] Zhaoxin Qiu,[1] Haiyang Chen,[1] Zhen Lingxuan[3]

[1]College of Mechanical and Electrical Engineering, Xinjiang Agricultural University, Urumqi; [2]Department of Biosystems Engineering, Zhejiang University, Hangzhou; [3]College of Electronic and Information Engineering, Southwest University, Chongqing, China

Abstract

This study proposes a navigation system for the headland autonomous turning of a safflower picking robot. The proposed system includes binocular cameras, differential satellites, and inertial sensors. The method of extracting the headland boundary line combining the hue, saturation, and value-fixed threshold segmentation method and random sample consensus algorithm and planning the headland-turning trajectory of a robot based on the multi-order Bezier curve are used as control methods. In addition, a headland-turning tracking model of a safflower picking robot is designed, and a path-tracking control algorithm is developed. A field test verifies the performance of the designed headland-turning navigation system. The test results show that the accuracy of the judgment result regarding the existence of a headland is higher than 96%. In headland boundary detection, the angle deviation is less than 1.5°, and the depth value error is less than 50 mm. The headland-turning path tracking test result shows that at a turning speed of 0.5 km/h, the average lateral deviation is 37 mm, and the turning time is 24.2 seconds. Compared to the 1 km/h, the turning speed of 0.5 km/h provides a better trajectory tracking effect, but the turning time is longer. The test results verify that this navigation system can accurately extract the headland boundary line and can successfully realise the headland-turning path tracking of a safflower picking robot. The results presented in this study can provide a useful reference for the autonomous navigation of a field robot.

Introduction

Safflower (*Carthamus tinctorius L.*) is an economic crop widely used for medicinal materials, oil plants, dyes, and feed (Mani *et al.*, 2020). Multiple batches characterise the safflower blooming, and the existence of different maturation stages of safflower filaments and seeds in safflower fruit bulbs makes mechanised harvesting challenging. Currently, the safflower picking process is dominated by manual picking, facing the problems of large labour demand, high labour intensity, high cost, and low efficiency (Yun *et al.*, 2016; Oyedeji *et al.*, 2022). Using a safflower picking robot can effectively solve these problems, so improving the precision and intelligence of the safflower harvesting operation is of high significance to increase production efficiency and economic benefits in the safflower industry.

Autonomous navigation is the basis for agricultural robots to realise field operations (Guevara *et al.*, 2020; Yin *et al.*, 2020). Field navigation of a safflower picking robot mainly includes inter-row navigation, automatic obstacle avoidance in the field, and automatic headland turning (Bulgakov *et al.*, 2021). Due to the high complexity, achieving an efficient automatic headland turning has become crucial for a safflower robot to realise autonomous navigation in the field (Sabelhaus *et al.*, 2013; Jing *et al.*, 2021). A headland environment where a safflower picking robot is located is dynamic and uncertain. In such an unstructured headland environment, it is necessary to obtain a headland's spatial position information to realise a robot's autonomous turning (Shalal *et al.*, 2015; Heiß *et al.*, 2019). The headland boundary line is a key parameter to describe the spatial position of a headland, and it is usually approximately linear in a short-distance range (Wang *et al.*, 2020). A safflower picking robot provides a turning reference line for subsequent planning of a headland-turn-

ing path by detecting the position of a headland boundary line.

Machine vision-based perception technology is an effective way to extract a headland boundary line. A headland boundary line can be obtained by segmenting and filtering a headland area image and then performing the headland boundary fitting (Jeon *et al*., 2021; Luo *et al*., 2022). Commonly used linear boundary extraction methods include Hough transform and the least squares method (LSM). Although Hough transform can detect straight lines in images effectively, its detection performance is limited by several factors, including time, space, and imaging noise. The LSM can rapidly extract the headland boundary line, but it is sensitive to noise, and it is challenging to accurately extract the boundary line in a noisy headland environment (Yin *et al*., 2018). Random sample consensus (RANSAC) has great advantages over the LSM, thus improving the computational efficiency and reliability in noisy environments, and the robustness and accuracy of boundary-line extraction (Zhou *et al*., 2021). He *et al*. (2022) adopted a multi-boundary detection method based on the frame correlation and RANSAC to detect farmland boundary lines and end boundaries. The angle error of boundary detection of less than 2° was achieved, and key information for agricultural machinery headland turning was provided. Turning path planning is the premise for realising the successful headland turning of a safflower picking robot (Ye *et al*., 2018; Zhang *et al*., 2022). The geometric trajectories used for path planning include line segment arcs, β splines, and Bezier curves (Ravankar *et al*., 2018). A Bezier curve represents a continuous smooth curve with the characteristics of continuous curvature, smooth motion, and simple control, and it has been widely used in many applications, including mobile-robot trajectory planning and mechanism motion planning (Duraklı and Nabiyev, 2022). Another challenge in headland turning is motion control because turning is often regarded as curve path tracking (Han *et al*., 2019). The methods of curve path tracking include retrospective predictive control, proportion integration differentiation (PID) control, fuzzy control, sliding mode control, and many others (Huan *et al*., 2020; Huang *et al*., 2021) . The PID control has been widely used due to its simplicity and robustness. Fuzzy PID represents a combination of fuzzy logic control and conventional PID, and it does not require establishing an accurate mathematical model and updates parameters according to actual working conditions (Abdelhakim and Abdelouahab, 2019). In addition, it has a small overshoot, a fast response speed, and a short time to achieve a stable state. Wang *et al*. (2018) proposed an algorithm for the adaptive turning of tractors on a headland. This algorithm uses a tractor's sliding motion and turning rate to adjust parameters based on the results of each turn. Test results showed that the average lateral deviation of a tractor's headland turning was less than 50 mm, and the turning time consumption was low. Mao *et al*. (2022) developed an autonomous robotic navigation system for orchard harvesting with a dual master-slave mode, where the cloth simulation filter (CSF) and RANSAC algorithms were used for navigation path construction. Also, a pure tracking algorithm was used to track the navigation path. The test results showed that the position deviations of the master and slave robots were less than 53 mm and 400 mm, respectively, which meets the requirements for positioning accuracy of an autonomous robot navigation system for double-master orchard harvesting.

This study presents a headland-turning navigation system for a safflower picking robot that combines the headland boundary line extraction method, turning path planning based on the Bezier curve, and the headland-turning path tracking control method. The field test verifies the performance of the proposed headland-turning navigation system.

Materials and Methods

Navigation system hardware

A headland-turning navigation system of a safflower picking robot includes three sensors, a set of differential drive devices, a controller, and an electric control cabinet, as shown in Figure 1. One of the sensors is the ZED2 binocular camera (Stereolabs, San Francisco, CA, USA), which is used to obtain headland boundary information. A binocular camera is installed in front of a robot on the centre line of the robot at the height of 1.7 m above the ground and an inclination of 65° to the ground. The second sensor is the HWT905 Inertial Measurement Unit (IMU) (Shenzhen Witt Intelligent Technology Co., Ltd., China), which is located in front of the robot to obtain high-precision, high-frequency information on the relative position and attitude of the robot through track estimation (Gai *et al*., 2021). The last sensor is the P3DU high-precision differential global navigation satellite system (DGNSS) satellite receiver (Shanghai Huace Navigation Technology Co., Ltd., China). This receiver is used to obtain signals from dual satellite antennas and the B5UA-CHOWYA base station (Shanghai Huace Navigation Technology Co., Ltd., China), which are then used to obtain the heading angle, latitude, and longitude of the robot. Dual satellite antennas are installed on the robot, one placed on the front, and another is behind the robot; they are 1.5 m apart and located 1.7 m from the ground.

The differential drive device includes a servo motor, a driver, a drive wheel, a reducer, and a transmission chain. The servo motor drives the drive wheel to perform differential motion through the reducer and transmission chain, realising the straightforward movement and turning of the robot. The controller is an APQ-E8 industrial computer (Chengdu Apqi Technology Co., Ltd., China), and it is installed in an electric control cabinet. The battery, satellite receiver, wireless access point (AP) radio and power conversion device are also installed in the electric control cabinet. The robot can interact with the dispatching system in real-time through the wireless AP radio, which is convenient for human-computer interaction during navigation.

The technical characteristics of the main components of the navigation system presented in Figure 1 are given in Table 1. All sensors have been calibrated by the supplier and tested by the authors. In addition, all sensors used in this study are following the corresponding product standards.

The controller uses the Linux operating system, and its hardware includes an Intel i7 processor, an 8-GB DDR4 memory, and a 128-GB solid-state disk. The RS232 serial port on the controller communicates with the satellite receiver; the USB 3.0 on the controller communicates with the ZED camera; the controller communicates with the IMU and servo motor of the differential drive through the controller area network bus (CAN Bus). Further, the controller analyses and processes data collected by the satellite receiver, ZED camera, and IMU in real time, perceives the robot and headland data and plans the turning path. In addition, the differential drive is controlled to track the headland-turning path so that the safflower picking robot can autonomously turn according to the headland information. The headland-turning control system is presented in Figure 2. The working principle of the headland-turning system is as follows. First, the satellite receiver, IMU, and ZED cameras obtain satellite positioning information, vehicle body attitude, and headland images. The controller processes the acquired data to construct a turning path, and then the rotational speed of the left and right driving wheels is obtained according to

the tracking situation of the turning path. Next, the obtained speed value is sent to the servo motor driver *via* the CAN bus to realise the differential turning control of a safflower picking robot. The wireless AP radio lets the controller interact with the dispatching system in real-time.

Headland-turning control method

The schematic diagram of the field navigation path of a safflower picking robot is shown in Figure 3. When a safflower picking robot reaches the turning start point, the inter-row navigation

program ends and the headland-turning program is triggered. After the robot reaches the turning endpoint, the headland-turning program is terminated, and the inter-row navigation program is executed. In this way, the autonomous field navigation of a safflower-picking robot is realised. This study primarily focuses on the headland turning of a safflower-picking robot. When a safflower picking robot reaches the turning start point, the headland point cloud information is obtained by the camera. Then, the threshold segmentation and RANSAC algorithm are employed to extract the headland boundary line, generating the turning reference line. The

Figure 1. Safflower picking robot structure: 1) binocular camera; 2) inertial measurement unit; 3) satellite antenna; 4) satellite base station; 5) satellite receiver; 6) industrial computer; 7) servo motor; 8) drive wheel.

Table 1. Technical characteristics of the main components of the navigation system.

Component	Performance	Value
Satellite receiver	RTK plane accuracy	$\pm(10+1\times10^{-6}\times d)$ mm
	Speed accuracy	0.03 m/s
	Yaw angle accuracy	(0.2/r)
	Data refresh frequency	20 Hz
ZED2 camera	Field of view	Max: 110°(H)×70°(V)×120°(D)
	Depth accuracy	<3%
	Focal length	2.12 mm
	Pixel size	2×2 μm
	Resolution	2688×1520
	Maximum frame rate	100 FPS
IMU	Acceleration range and accuracy	±6 g, 0.01 g
	Angular velocity range and accuracy	2,000°/s, 0.05°/s
	Data refreshing frequency	200 Hz

d, linear distance between the positioning antenna and the base station expressed in km; r, linear distance between the two positioning antennas given in m; H, horizontal viewing angle; V, vertical viewing angle; D, diagonal viewing angle; RTK, real time kinematic; IMU, inertial measurement unit.

turning feature points are obtained based on the turning reference line, and the turning path is designed based on a Bezier curve. Information on lateral deviation, angular deviation, and speed information is obtained from the positioning data of the sensors, and the fuzzy PID control algorithm is used to track the Bessel turning path. When a safflower picking robot reaches the turning endpoint along the Bezier turning path, the robot posture is adjust-

ed, the robot enters the inter-row along the ridge, and the inter-row navigation program is executed.

The safflower planting mode includes both wide and narrow-row drill planting types. The safflower row spacing l_1 is 1 m, the wide row distance l_2 is 0.55 m, the narrow row distance is 0.45 m, and the headland distance d_3 is 4 m. The flowchart of a safflower picking robot's headland-turning process is shown in Figure 4.
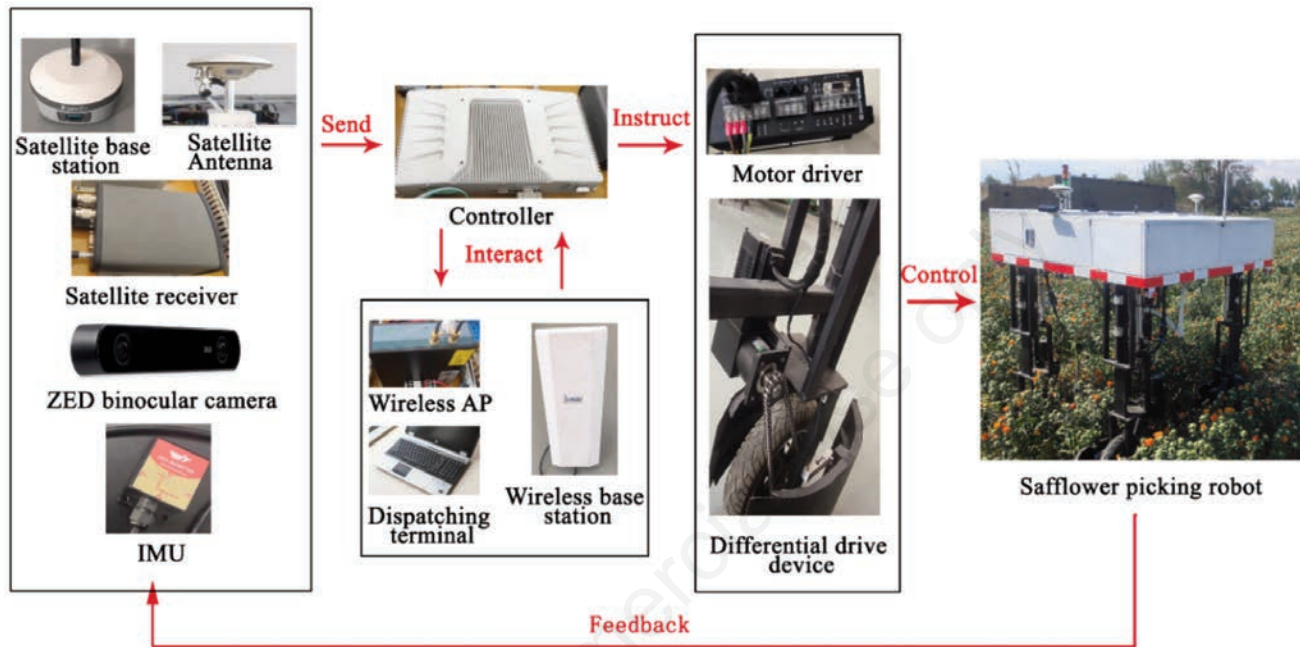
Figure 2. Headland-turning control system. IMU, inertial measurement unit.
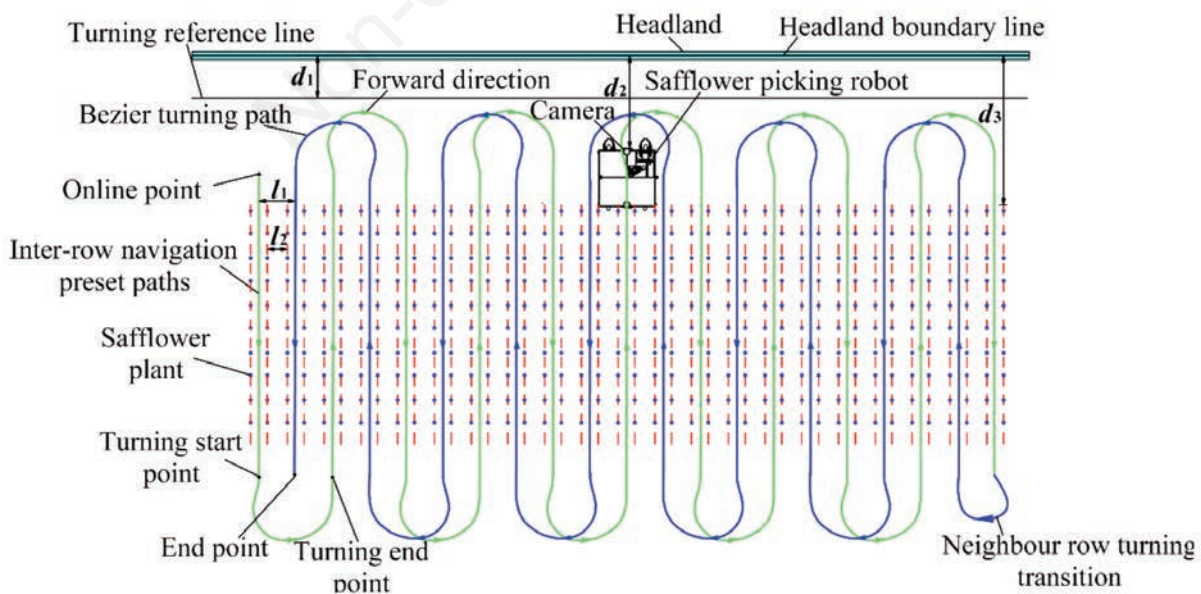
Figure 3. Schematic diagram of the field navigation path of a safflower picking robot.

Identification and positioning of headland boundaries

Before safflower picking robot turns to a headland, it needs to judge whether there is a headland in its field of vision. Only when a headland has been detected the process of headland boundary identification and positioning is performed. The headland boundary identification and positioning process mainly includes five steps: threshold segmentation from a headland image, sharpening filtering, boundary feature point extraction, boundary line fitting, and headland depth value determination. The process of identifying and positioning a headland boundary line is shown in Figure 5. The left camera of the ZED2 binocular camera takes the original image. Threshold segmentation is a process of image segmenting into objects and backgrounds according to a preset threshold T; in this process, selecting a suitable threshold value is crucial. In this study, the hue, saturation, and value (HSV)-fixed threshold segmentation method are employed to realise threshold-based image segmentation. Compared with the RGB mode, the HSV model can significantly reduce the influence of illumination and impurities on the image segmentation result (Fu *et al*., 2020). In the HSV-based methods, first, the original image of a headland is cross-sectioned, the grey value of a headland pixel is analysed, and statistics obtains the HSV component of a section line pixel. The value ranges of the H, S, and V components are [40, 150], [30, 40], and [80, 150], respectively. The threshold segmentation process is performed based on the value ranges of the HSV components.

After the image threshold segmentation is conducted, feature points are sharpened and filtered. In this study, the Laplacian sharpening filter is used for filtering because this filter can segregate areas of rapidly-changing pixel values. Using this filter, the headland information can be highlighted, the blurred headland outline information can be cleared, and the headland recognition quality can be improved. After an image is sharpened and filtered, all feature points are scanned, and two-dimensional coordinates of all feature points are obtained. The RANSAC algorithm is used to sample images multiple times randomly to establish a linear estimation model and then to calculate the number of inliers contained in the model. Multiple iterations are performed to obtain a linear model with the most interior points representing the headland boundary line. According to the two-dimensional coordinates of
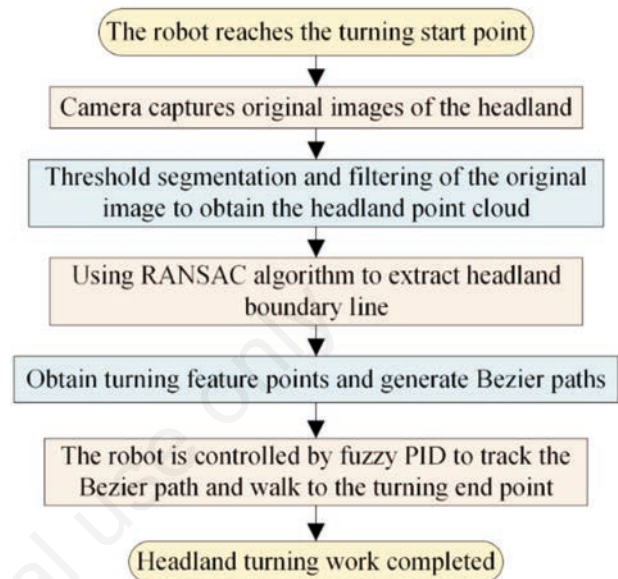
Figure 4. The flowchart of the headland-turning process. RANSAC, random sample consensus; PID, proportion integration differentiation.
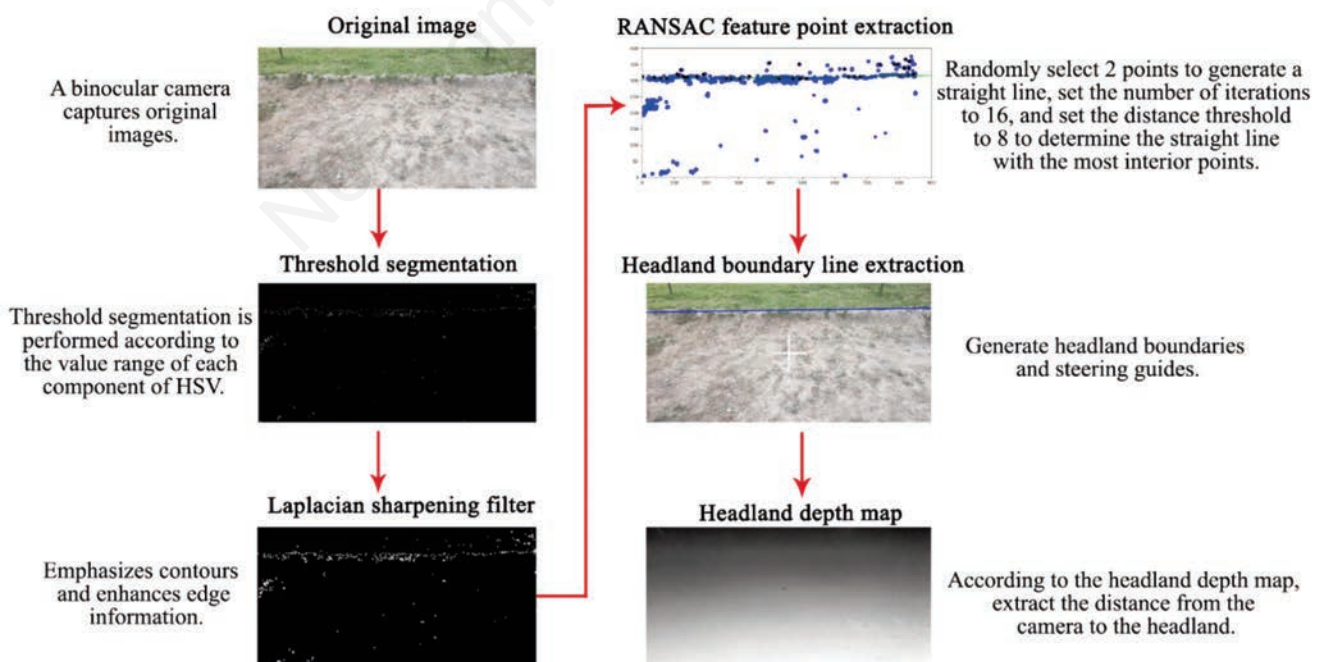
Figure 5. The process of identifying and positioning a headland boundary line. RANSAC, random sample consensus; HSV, hue, saturation, and value.

the feature points on the headland boundary line and headland depth map, the depth value d_2 from the camera to the headland boundary line is calculated, as shown in Figure 3.

The schematic diagram of headland positioning is shown in Figure 6.

The headland depth map refers to an image where the distance (depth) from the camera to each point in the headland scene is represented as a pixel value. The headland depth map is obtained through stereo matching, using the left ZED2 camera data as a reference. Assume that the projection point of the camera on the ground denotes the coordinate origin O_w; the direction perpendicular to the outside of the robot platform is the X_w axis; the robot's forward direction is the Z_w axis; the connection direction between the coordinate origin and the camera is the Y_w axis. Then, the conversion formula between the camera coordinate system, and the global coordinate system is given by Eq. 1:

$$\begin{bmatrix} X_w \\ Y_w \\ Z_w \\ 1 \end{bmatrix} = \begin{bmatrix} 1 & 0 & 0 & 0 \\ 0 & -cos\theta & -sin\theta & h \\ 0 & -sin\theta & cos\theta & 0 \\ 0 & 0 & 0 & 1 \end{bmatrix} \begin{bmatrix} X_c \\ Y_c \\ Z_c \\ 1 \end{bmatrix} \quad (1)$$

where (X_w, Y_w, Z_w) denotes the coordinates of a pixel in the global coordinate system; (X_c, Y_c, Z_c) are the coordinates of the pixel in the camera coordinate system; θ is the rotation angle between the camera coordinate system, and the global coordinate system; and h is the translation distance from the camera coordinate system to the global coordinate system in the vertical direction.

Through coordinate transformation, the depth value obtained by the camera in the camera coordinate system is converted into a distance (d_2) from the camera to the headland in the global coordinate system.

Random sample consensus boundary line fitting

The RANSAC linear fitting method is used to extract the headland boundary line. The RANSAC method differs from the least squares method, which uses all sample data to estimate model parameters. Namely, the RANSAC method samples data multiple times randomly and then, also randomly, selects a few sample points to estimate model parameters. The estimated model parameters are further used to divide the remaining sample points into two categories: interior points that satisfy the mathematical model and outer points that do not satisfy the mathematical model (Ericson and Astrand, 2018). After multiple random sampling, model parameters are obtained with a small error.

The RANSAC headland boundary line fitting steps are as follows. First, two points are randomly selected from the detected headland boundary point cloud and connected to obtain a straight line. Next, the slope of the straight line is estimated to decide whether to keep it or not. Then, the distance threshold t_d is set, and the distance from the remaining points to the straight line is calculated, which is further used to classify points into inner and outer points. As such, points with a distance less than t_d are regarded as inner points, and feature points whose distance is larger t_d are regarded as outer points.

Further, all feature points are traversed, and the number of interior points in the model is determined. Afterward, the iteration threshold K is set, and the above process is repeated K times. Finally, the line corresponding to the model with the largest number of interior points is selected as the best headland boundary line.

The iteration threshold K is a crucial parameter of the fitting process. If the value of K is too large, the above process becomes too time-consuming; in contrast, if the value of K is too small, the fitting effect is poor. According to the related literature (Zhou et al., 2021), the more appropriate value of K is obtained by Eq. 2:

$$K = \frac{lg\ (1-\alpha)}{lg\ (1-\lambda^N)} \quad (2)$$
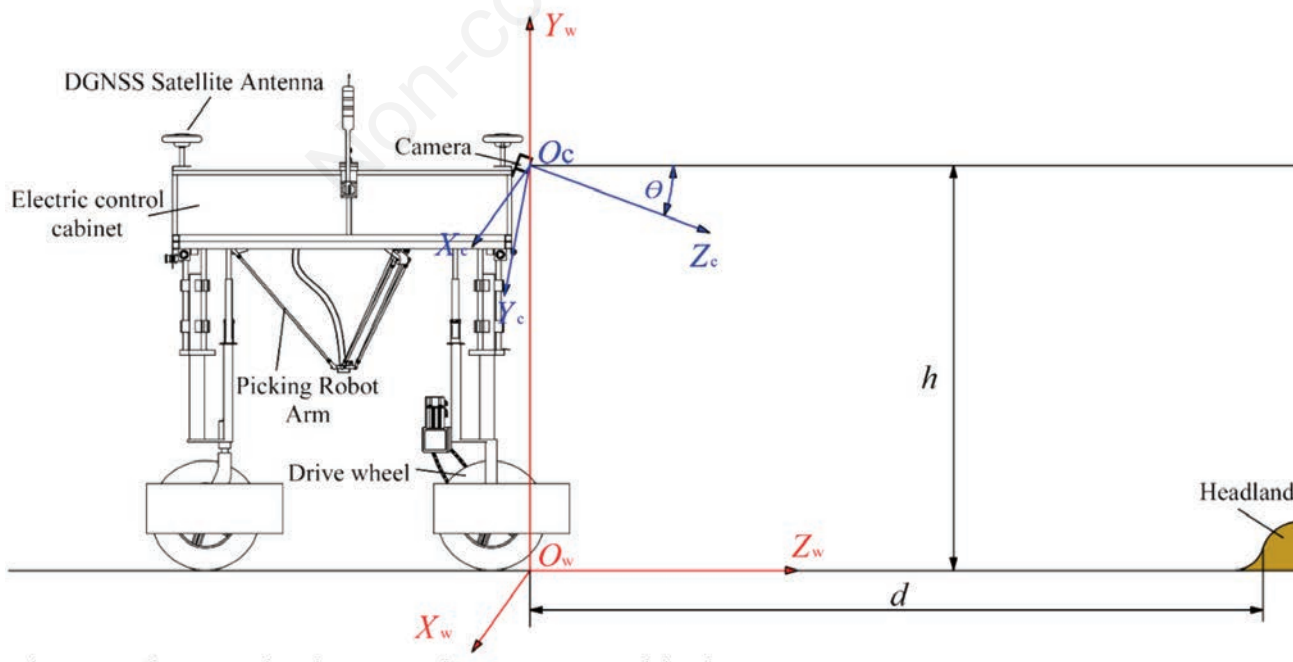
Figure 6. Schematic diagram of headland positioning.

where α is the probability that the RANSAC algorithm obtains the correct result, expressed in percent; λ is the probability of selecting a point from data as an interior point, also expressed in percent; N is the minimum number of feature points required to estimate model transmission.

Theoretically, if the proportion of abnormal data points is less than 50% of the total data points, the RANSAC algorithm can achieve good results. Therefore, in this study, the value of λ is set to 0.5; α is set to 0.99, and N has a value of two. The final iteration threshold K is 16, the distance threshold t_d is eight, and the slope range of the headland boundary line is -1, 1.

Bezier turning path planning

In this work, the turning trajectory of a safflower picking robot is planned based on a multi-order Bezier curve, as shown in Figure 7. The turning path based on a Bezier curve can satisfy the continuity requirement of a turning path and reduce the computational complexity of a controller (Backman *et al.*, 2015). A Bezier curve is defined by a set of control points connected in sequence to form a polygon. The shape of a Bessel curve is changed by adjusting the coordinates of control points so that the curve approximates the polygon continuously (Li *et al.*, 2019). For an n-order Bezier curve, $(n+1)$ control points $(P_0, P_1, ..., P_n)$ should be determined. The parametric equation of a Bezier curve is as follows (Eq. 3):

$$B(t) = \sum_{i=0}^{n} Q_{i,n}(t)P_i, t \in [0,1] \tag{3}$$

where P_i ($i = 0, 1,..., n$) denotes the coordinates of the ith control point, and the polyline connecting points from P_0 to P_n in sequence constitute a control polygon of the Bezier curve.

The basis function $Q_{i,n}(t)$ is a Bernstein polynomial, which is given by Eq. 4:

$$Q_{i,n}(t) = \frac{n!}{i!(n-i)!} t^i (1-t)^{n-i} \tag{4}$$
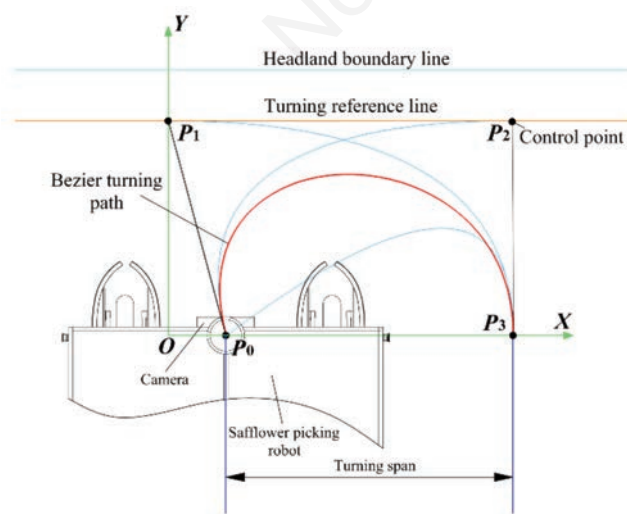
This paper used a third-order Bezier curve to generate a smooth path. As mentioned before, for a third-order Bezier curve, it is necessary to determine four control points (P_0, P_1, P_2, P_3), where P_0 is the turning start point, point P_3 is the turning end point, and points P_1 and P_2 are process control points whose coordinates are defined by the turning reference line and turning span.

Headland path tracking control

The geometric illustration of the Bezier turning control is displayed in Figure 8, where EF is the planned partial Bezier path. Assume that a differential drive robot makes a right turn at the headland. The centre of the two driving wheels of the robot represents the positioning point. A collection of navigation points describes a Bezier path, and the real-time information on the robot's position and angle is obtained by the DGNSS and inertial navigation.

The path-tracking method of the turning controller is as follows. First, the navigation controller determines the closest point to the robot on the planned path and calculates the radial deviation δ. Then, the Euclidian distance between this point and the robot is calculated. When a robot performs the right-turning path tracking, if the robot is on the left side, then $\delta>0$, but if the robot is on the right side of the path, then $\delta<0$. Next, the robot starts at point A and the look-ahead point B is obtained by moving a constant number of navigation points from point A along the planned path. Similarly, point C is obtained by moving by the same number of navigation points from point B. The forward direction of point B is the line direction V_B of BC, and the speed direction V_A of the robot at point A is mapped to point B as V_A'; the angle between V_A' and V_B represents the angular deviation θ. When the angular deviation is left relative to the target heading, the heading angle is negative, and $\theta<0$; the heading angle is positive when the angular deviation is right relative to the target heading, and $\theta>0$. Finally, when the robot turns a headland, the vehicle body path tracking control is realised based on the speed difference of the driving wheels and reducing the value of the look-ahead points δ and θ.

The robot path-tracking control is based on a combination of incremental PID and fuzzy control. The control increment $\Delta u(k)$ is

Figure 7. Schematic diagram of a Bezier turning path.
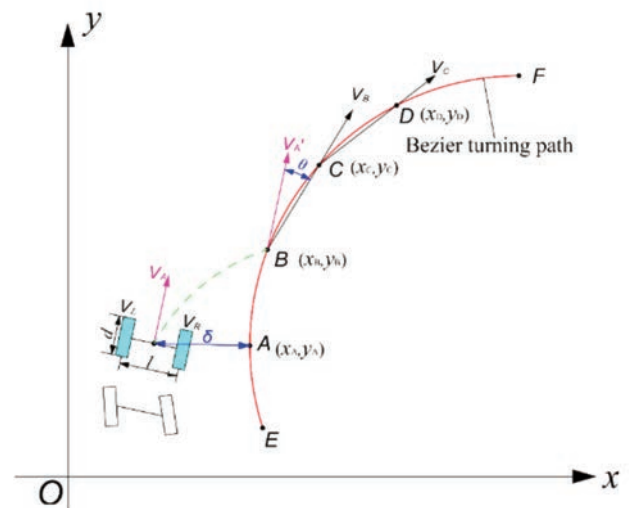
Figure 8. Bezier turning control process illustration.

obtained using only the last three sampling values, and a good control effect can be achieved by weighting. Unlike positional PID, incremental PID does not accumulate the integral term, so it will not affect the system's operation and control. Therefore, incremental PID achieves better control quality than positional PID (Tang *et al.*, 2020). The control quantity is obtained by Eq. 5:

$$u(k) = K_P e(k) + K_I \sum_{i=0}^{k} e(i) - K_D [e(k) - e(k-1)] \quad (5)$$

where $e(k)$ is the control deviation at the k sampling time; K_P is the proportional coefficient; K_I is the integral coefficient; and K_D is the differential coefficient.

The control increment $\Delta u(k)$ can be calculated as follows (Eq. 6):

$$\begin{cases} \Delta(k) = u(k) - u(k-1) \\ \Delta(k) = K_P[e(k) - e(k-1)] + K_I e(k) + K_D[e(k) - 2e(k-1) + e(k-2)] \end{cases} \quad (6)$$

The input variables δ and θ and output variables K_P, K_I, and K_D are fuzzified. According to the position of the picking robot wheel between the safflower rows, the value ranges of δ and θ are -100 mm -100 mm and -45°-45°, respectively. To simplify the calculation, values of lateral and angular deviations (*i.e.*, δ and θ) are divided into seven fuzzy subsets: negative big (*NB*), negative medium (*NM*), negative small (*NS*), zero (*ZO*), positive small (*PS*), positive medium (*PM*), and positive big (*PB*), and the corresponding quantification level is expressed as follows (Eq. 7):

$$[-6, -4, -2, 0, 2, 4, 6] = [NB, NM, NS, ZO, PS, PM, PB] \quad (7)$$

The lateral and angular deviation quantization factors, K_a and K_b, are 1/30 and 1/15, respectively. The actual value ranges of the output variables K_P, K_I, and K_D of the fuzzy controller are set to [-5, 5], [-0.01, 0.01], and [-3, 3], respectively. Considering the real-time and complexity of the control system, the navigation system adopts a triangular membership function, and the parameter adaptation formula is given by (Garcia-Martinez *et al.*, 2020) (Eq. 8):

$$\begin{cases} K_P(k) = K_{P0} + \Delta K_P(k) \\ K_I(k) = K_{I0} + \Delta K_I(k) \\ K_D(k) = K_{D0} + \Delta K_D(k) \end{cases} \quad (8)$$

where K_{P0}, K_{I0}, and K_{D0} are the initial values of PID parameters, and $K_P(k)$, $K_I(k)$, and $K_D(k)$ are the three outputs of the fuzzy controller.

The fuzzy controller adopts the centre of gravity (COG) method to defuzzify the fuzzy subsets (Sain and Mohan, 2021). The defuzzification process uses a weighted average to obtain the precise values of the three PID tuning parameters output after defuzzification. The fuzzy PID controller adjusts ΔK_P, ΔK_I, and ΔK_D in real-time according to the headland path tracking position, thereby achieving the adaptive tuning of K_P, K_I, and K_D.

Results and Discussion

Headland identification and positioning test

The headland identification and positioning test was performed from June 7 to 13, 2022, at the safflower plantation of Hongqi Farm, Jimsar County, Changji City, Xinjiang, China. According to the safflower crop management operation and general robot turning navigation requirements, the ZED camera's installation height was set to 1700±5 mm, and the pitch angle was 65±3°. After the safflower picking robot reached the turning point, it detected the headland boundary line. Only when the headland boundary line could be detected, and the detected headland boundary line could ensure safe and reliable autonomous turning of the robot, the detection of the headland boundary line was considered correct. The resolution of all images was 1280×720 pixels, the weather was clear during picture collection, and the time period was 9-11 a.m. and 3-5 p.m. The headland boundary monitoring process is shown in Figure 9.

The detection results of the headland boundary line are shown in Table 2. The detection items included judgment on the headland existence, and the headland boundary line detection was based on the headland detection result.

As shown in Table 2, the accuracy rate of the judgment on the headland existence was higher than 96%, and the detection accuracy of the headland boundary line was higher than 93%. The image processing time by the Python-OpenCV regarding the headland existence was less than 0.6 seconds, and the image processing time for the headland boundary line detection was less than 1 second. The angular deviation of the headland boundary line detection was less than 1.5°, and the depth error was lower than 50 mm. The test results showed that the proposed algorithm could accurately judge

Figure 9. Headland boundary monitoring process: a) with vegetation cover; b) without vegetation cover.

whether there was a headland and could rapidly detect the headland boundary line necessary for the autonomous navigation of a robot. The detected headland boundary line ensured that the robot was within the turning reference line and could complete the turning operation safely and reliably.

Turning path tracking test

A headland-turning path tracking test was conducted at different speeds to test the accuracy and robustness of headland-turning path tracking. The test was performed from July 2 to 11, 2022, and the test site was the safflower plantation of Hongqi Farm, Jimsar County, Changji City, Xinjiang. The road in the safflower plantation was flat, and the safflower picking robot was a span-row turning. The safflower row spacing was 1 m, the turning span was 2 m, and the headland width was 3 m. The headland-turning path tracking test was conducted at 1 km/h and 0.5 km/h speeds. The headland-turning path-tracking process of a safflower picking robot is presented in Figure 10. After the robot reached the turning point, it monitored the headland boundary line to obtain the turning feature

points and used the third-order Bezier algorithm to create a Bezier turning preset path. The robot tracked the turning path defined by the preset path. The preset path and the actual position of the robot are shown in Figure 11.

The values of the lateral deviation δ and angular deviation θ of the robot along the headland-turning path at different speeds are presented in Figure 11. When the safflower picking robot reached the turning starting point at a speed of 1 km/h, the lateral deviation was 26 mm, and the angular deviation was 1.2°; however, at a speed of 0.5 km/h, the lateral deviation was 17 mm, and the angular deviation was 0.8°. This indicated that the transition from the straight path to the headland-turning path was smooth at both speeds. The numerical results obtained at different turning speeds of the safflower picking robot are given in Table 3.

The field test results showed that when the turning speed of the safflower picking robot was 1 km/h and the robot reached the turning end point, the lateral and angular deviations were 34 mm and 2.5°, respectively. However, at the turning speed of 0.5 km/h, when the robot reached the turning end point, the lateral and angular

Table 2. The detection results of the headland boundary line.

Parameter		Vegetation covered headland	Non-vegetation covered headland
Judgment result on the headland existence	Number of images	200	200
	Single image processing time (s)	0.54	0.53
	Accuracy (%)	98	96
Headland boundary line detection	Number of images	196	192
	Single image processing time (s)	0.81	0.94
	Accuracy (%)	96	93
	Angular deviation (°)	1.1	1.3
	Depth value error (mm)	37	48
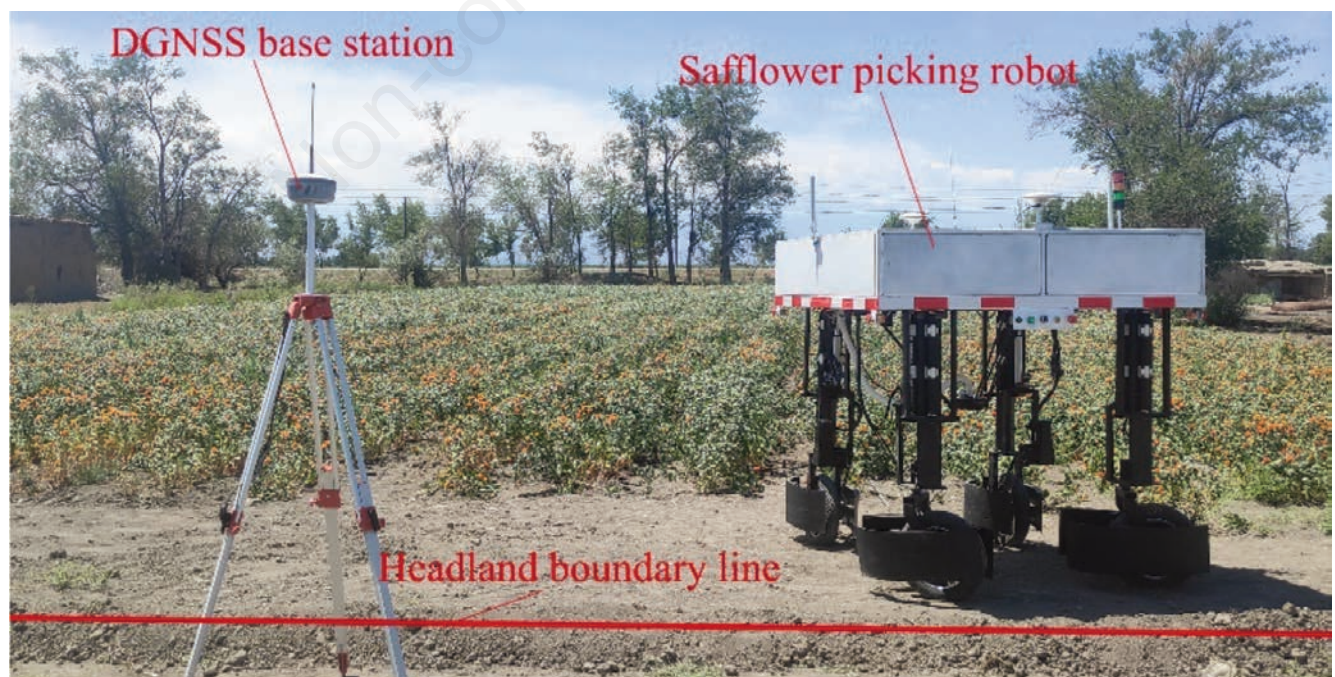
Figure 10. Turning path tracking process. DGNSS, differential global navigation satellite system.

Table 3. Comparison results of the safflower picking robot at different turning speeds.

Turning speed (km·h⁻¹)	Turning starting point		Turning end point		Maximum lateral deviation (mm)	Mean lateral deviation (mm)	Time consumption (s)
	δ (mm)	θ (°)	δ (mm)	θ (°)			
1	26	1.2	34	2.5	115	53	13.6
0.5	17	0.8	18	1.3	88	37	24.2
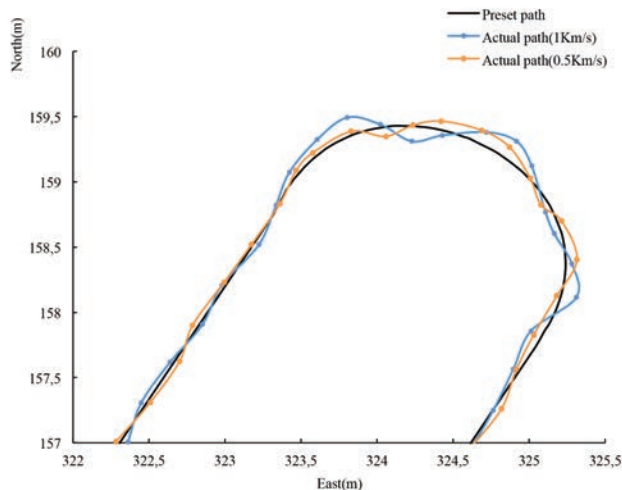
Figure 11. The preset path and actual position of a robot.

deviations were 18 mm and 1.3˚, respectively. Therefore, for the turning speed of the safflower picking robot of 1 km/h and 0.5 km/h, the headland-turning task could be successfully completed. Compared to the 1 km/h, the turning speed of 0.5 km/h had smaller maximum and average lateral deviations and a better trajectory tracking effect, but the turning time was longer. The test results show that the proposed incremental fuzzy PID automatic turning control system had high tracking accuracy and good robustness and could meet the field headland-turning requirements of a safflower picking robot.

Conclusions

This paper presents the navigation system that can meet the headland-turning requirements of a safflower picking robot. The proposed system can realise headland boundary line extraction, headland-turning path planning, and turning path tracking of a safflower picking robot. This navigation system can also realise human-computer interaction in the machine monitoring process. Using the proposed system, the reliability and adaptability of the headland-turning process of a safflower picking robot are improved, which can provide a valuable reference for the headland turning of a field operation robot.

The headland identification and positioning test verifies the proposed system. The image processing time of headland boundary line detection is less than 1 second, the angular deviation of headland boundary line detection is less than 1.5˚; the depth value

error is lower than 50 mm. The test results also show that the proposed system can accurately judge whether there is a headland and can rapidly detect the headland boundary line, which is then used for the autonomous navigation of a robot. The detected headland boundary line can ensure that the robot is within the turning reference line, and then the turn-around operation can be successfully completed safely and reliably.

According to the turning path tracking test results, the safflower picking robot can complete the headland-turning task effectively at the turning speeds of 1 km/h and 0.5 km/h. At the turning speed of 0.5 km/h, the average lateral deviation is 37 mm; the turning time is 24.2 seconds. After the robot reaches the turning end point, the lateral and angular deviations are 18 mm and 1.3˚, respectively. The proposed headland-turning control system has high tracking accuracy and good robustness and can meet the field headland-turning requirements of a safflower picking robot.

The challenges in the autonomous turning control of safflower picking agricultural robots are designing a feasible navigation path and developing adaptive control technology. A control algorithm needs to adapt to dynamic changes in soil conditions to ensure stable control performance. The main research direction in optimisation of the headland-turning control of agricultural robots is to reduce turning time, turning path, and power consumption of the headland-turning process while improving the headland-turning efficiency.

References

Abdelhakim G., Abdelouahab H. 2019. A new approach for controlling a trajectory tracking using intelligent methods. J. Electr. Eng. Technol. 14:1347-56.

Backman J., Piirainen P., Oksanen T. 2015. Smooth turning path generation for agricultural vehicles in headlands. Biosyst. Eng. 139:76-86.

Bulgakov V., Pascuzzi S., Ivanovs S., Kuvachov V., Postol Y., Santoro F., Melnyk V. 2021. Study of the steering of a wide span vehicle controlled by a local positioning system. J. Agric. Eng. 52.

Duraklı Z., Nabiyev V. 2022. A new approach based on Bezier curves to solve path planning problems for mobile robots. J. Comput. Sci-Neth. 58:101540.

Ericson S.K., Astrand B.S. 2018. Analysis of two visual odometry systems for use in an agricultural field environment. Biosyst. Eng. 166:116-25.

Fu L., Majeed Y., Zhang X., Karkee M., Zhang Q. 2020. Faster R-CNN-based apple detection in dense-foliage fruiting-wall trees using RGB and depth features for robotic harvesting. Biosyst. Eng. 197:245-56.

Gai J.Y., Xiang L.R., Tang L. 2021. Using a depth camera for crop row detection and mapping for under-canopy navigation of

agricultural robotic vehicle. Comput. Electron. Agr. 188: 106301.

Garcia-Martinez J.R., Cruz-Miguel E.E., Carrillo-Serrano R.V., Mendoza-Mondragon F., Toledano-Ayala M., Rodriguez-Resendiz J. 2020. A PID-type fuzzy logic controller-based approach for motion control applications. Sensors 20:5323.

Guevara C.L., Michalek M.M., Auat Cheein F. 2020. Headland turning algorithmization for autonomous N-trailer vehicles in agricultural scenarios. Comput. Electron. Agr. 175:105541.

Han X., Kim H.J., Jeon C.W., Moon H.C., Kim J.H., Yi S.Y. 2019. Application of a 3D tractor-driving simulator for slip estimation-based path-tracking control of auto-guided tillage operation. Biosyst. Eng. 178:70-85.

He Y., Zhang X.Y., Zhang Z.Q., Fang H. 2022. Automated detection of boundary line in paddy field using MobileV2-UNet and RANSAC. Comput. Electron. Agr. 194:106697.

Heiß A., Paraforos D., Griepentrog H. 2019. Determination of cultivated area, field boundary and overlapping for a plowing operation using ISO 11783 communication and D-GNSS position data. Agriculture 9:38.

Huan P., Zhang Z., Luo X. 2020. Feedforward-plus-proportional-integral-derivative controller for agricultural robot turning in headland. Int. J. Adv. Robot. Syst. 17.

Huang P., Zhu L., Zhang Z., Yang C. 2021. Row end detection and headland turning control for an autonomous banana-picking robot. Machines 9:103.

Jeon C., Kim H.J., Yun C., Han X., Kim J.H. 2021. Design and validation testing of a complete paddy field-coverage path planner for a fully autonomous tillage tractor. Biosyst. Eng. 208:79-97.

Jing Y., Liu G., Luo C. 2021. Path tracking control with slip compensation of a global navigation satellite system based tractor-scraper land levelling system. Biosyst. Eng. 212:360-77.

Li H., Luo Y., Wu J. 2019. Collision-free path planning for intelligent vehicles based on Bézier curve. Ieee Access. 7:123334-40.

Luo Y., Wei L., Xu L., Zhang Q., Liu J., Cai Q., Zhang W. 2022. Stereo-vision-based multi-crop harvesting edge detection for precise automatic steering of combine harvester. Biosyst. Eng. 215:115-28.

Mani V., Lee S.K., Yeo Y., Hahn B.S. 2020. A metabolic perspective and opportunities in pharmacologically important safflower. Metabolites 10:253-70.

Mao W., Liu H., Hao W., Yang F., Liu Z. 2022. Development of a combined orchard harvesting robot navigation system. Remote Sens. 14:675.

Oyedeji A.N., Ali Umar U., Shettima Kuburi L., Edet A.A., Mukhtar Y. 2022. Development and performance evaluation of an oil palm harvesting robot for the elimination of ergonomic risks associated with oil palm harvesting. J. Agric. Eng. 53.

Ravankar A., Ravankar A.A., Kobayashi Y., Hoshino Y., Peng C.C. 2018. Path smoothing techniques in robot navigation: state-of-the-art, current and future challenges. Sensors 18:3170.

Sabelhaus D., Röben F., Meyer zu Helligen L.P., Schulze Lammers P. 2013. Using continuous-curvature paths to generate feasible headland turn manoeuvres. Biosyst. Eng. 116:399-409.

Sain D., Mohan B.M. 2021. Modeling, simulation and experimental realization of a new nonlinear fuzzy PID controller using center of gravity defuzzification. ISA Trans. 110:319-27.

Shalal N., Low T., McCarthy C., Hancock N. 2015. Orchard mapping and mobile robot localisation using on-board camera and laser scanner data fusion - part B: mapping and localisation. Comput. Electron. Agr. 119:267-78.

Tang W., Wang L., Gu J., Gu Y. 2020. Single neural adaptive PID control for small UAV micro-turbojet engine. Sensors 20:345.

Wang Q., Liu H., Yang P., Meng Z. 2020. Detection method of headland boundary line based on machine vision. Trans. Chinese Soc. Agric. Mach. 51:18-27. [Article in Chinese].

Wang H., Noguchi N. 2018. Adaptive turning control for an agricultural robot tractor. Int. J. Agr. and Biol. Eng. 11:113-9.

Ye Y., He L., Wang Z., Jones D., Hollinger G.A., Taylor M.E., Zhang Q. 2018. Orchard manoeuvring strategy for a robotic bin-handling machine. Biosyst. Eng. 169:85-103.

Yin X., Du J., Noguchi N., Yang T., Jin C. 2018. Development of autonomous navigation system for rice transplanter. Int. J. Agr. Biol. Eng. 11:89-94.

Yin X., Wang Y., Chen Y., Jin C., Du J. 2020. Development of autonomous navigation controller for agricultural vehicles. Int. J. Agr. Biol. Eng. 13:70-6.

Yun G., Lixin Z., Ying Q., Xiaopan J., Yuanbo C. 2016. Dynamic model for sucking process of pneumatic cutting-type safflower harvest device. Int. J. Agr. Biol. Eng. 9:43-50.

Zhang T., Jiao X., Lin Z. 2022. Finite time trajectory tracking control of autonomous agricultural tractor integrated nonsingular fast terminal sliding mode and disturbance observer. Biosyst. Eng. 219:153-64.

Zhou M., Xia J., Yang F., Zheng K., Hu M., Li D., Zhang S. 2021. Design and experiment of visual navigated UGV for orchard based on Hough matrix and RANSAC. Int. J. Agr. Biol. Eng. 14:176-84.